



The role of lanthanum in the enhancement of photocatalytic properties of TiO₂ nanomaterials obtained by calcination of hydrogenotitanate nanotubes

Manel Meksi^a, Asma Turki^a, Hafedh Kochkar^{a,b,*}, Latifa Bousselmi^c, Chantal Guillard^d, Gilles Berhault^d

^a Université de Tunis El Manar, Faculté des Sciences de Tunis, Laboratoire de Chimie des Matériaux et Catalyse, 2092 Tunis, Tunisie

^b Centre National des Recherches en Sciences des Matériaux, Technopôle de Borj-Cédria, Soliman, Tunisie

^c Centre de Recherches et des Technologies des Eaux, Technopôle de Borj-Cédria, Soliman, Tunisie

^d Institut de Recherches sur la Catalyse et de l'Environnement de Lyon, CNRS - Université Lyon I, 69100 Villeurbanne, France

ARTICLE INFO

Article history:

Received 23 May 2015

Received in revised form 18 August 2015

Accepted 24 August 2015

Available online 28 August 2015

Keywords:

Titanate nanotubes

Lanthanum

Crystallite size

Oxygen vacancy

Photocatalysis

ABSTRACT

The influence of lanthanum on the thermal stability and photocatalytic activity of calcined hydrogenotitanate nanotubes (HNT) was herein evaluated. HNT samples were prepared through the hydrothermal treatment of TiO₂ P25 in a concentrated NaOH solution (11.25 M) at 130 °C during 20 h followed by acid washing. La-doped titanates nanotubes (La-HNT) photocatalysts with optimum 1 wt% of La were then elaborated by incipient wetness impregnation method using lanthanum nitrate as precursor. La-HNT and HNT samples were then calcined at temperatures varying between 400 °C and 700 °C. Samples were characterized by means of nitrogen adsorption–desorption isotherms at 77K, X-ray diffraction (XRD), Raman spectroscopy, diffuse reflectance spectroscopy (DRS), photoluminescence spectroscopy (PL), transmission electron microscopy (TEM), ICP analysis and photocurrent experiments. The photocatalytic activities of La-HNT and HNT derived nanomaterials were then evaluated through the photocatalytic degradation of formic acid (FA).

Main results reveal that lanthanum inhibits TiO₂ crystallite growth and retards anatase transformation into the less active rutile phase. The addition of La ions to TiO₂ results in a charge imbalance creating a high proportion of oxygen vacancies as evidenced by photocurrent, photoluminescence and Raman experiments.

The photocatalytic experiments reveal that La-doped TiO₂ helps to maintain a high photocatalytic activity level even after calcination at high temperatures contrary to La-free photocatalysts. The determination of kinetic parameters reveals that the maintaining of a high photocatalytic activity results from the synergetic effect between restriction of TiO₂ crystallite size growth and formation of a high proportion of oxygen vacancies.

© 2015 Elsevier B.V. All rights reserved.

1. Introduction

The development of heterogeneous photocatalysis was a great challenge in the last few decades especially using techniques involving TiO₂ as a semiconductor [1–3]. However, undesirable recombination of electrons and holes is considered as one of the main limiting step of this process. Yu et al. [4] showed that anatase phase is more active than rutile because it has a large number of hydroxyl groups (–OH) and higher specific surface area. The kinetic

of degradation of some pollutants may vary as a function of the photocatalyst type [5,6]. In fact, Araña et al. [7] and Liu et al. [8] showed that the photocatalytic activity depends on the crystallite size of anatase and the determination of the optimal size would minimize recombination reactions. Interestingly, the hydroxylated surface of the catalyst may also affect the photocatalytic activity. The hydroxyl groups are essential in the mechanism of photodegradation [9] since they play the role of adsorption sites for molecules that tend to form hydrogen bonds. Regarding texture, the specific surface area of the catalyst is a very interesting parameter in photocatalysis taking into account the fact that the kinetics of a heterogeneous reaction depends on the number of surface active sites [10]. Indeed, the specific surface area is proportional to the particle size and

* Corresponding author. Fax: +216 79 32 53 14.

E-mail address: h.kochkar@yahoo.fr (H. Kochkar).

plays an important role in the catalyst/pollutant interactions. It has been shown that the higher the surface area, the more pollutants can be adsorbed on the catalyst surface and can react rapidly with hydroxyl radicals formed on the TiO_2 surface [11]. In other words, the morphology, particle size and pore volume, which are related to the surface area, are very important parameters strongly influencing the performance of the photocatalyst. Nevertheless, the anatase crystallites sizes tend to grow by agglomeration after heat treatment and reach the critical germ size (≈ 14 nm) above which thermodynamic transition to the more stable rutile phase is favored [4]. This transition also creates more oxygen defects. In order to restrain TiO_2 crystallite growth, numerous studies were devoted to the doping of TiO_2 nanomaterials with non-metals species such as B, N, C, F [12] or metals ions such as Fe, Ag and Pt [13]. The metal ion 'dopant' (usually in its highest oxidation state) can act as a mediator and increase the photocatalytic efficiency or can act as recombination centers and decrease the photocatalytic activity. Therefore, conflicting reports exist in the literature regarding the photocatalytic activities on semiconductors doped with transition metal ions. The discrepancies are due to a number of factors that include, variability in the synthetic procedures employed for the preparation of catalysts that lead to the formation of photocatalysts with varying physico-chemical characteristics, varying experimental conditions used in the photocatalytic reactions (intensity of lamp, reactor geometry, wavelength of light used) and the different quantitative methods used for analysis of reactant and/or product concentrations [14]. Recent literature data contains several reports of doping with metal ions with enhanced activities compared to non-doped or pure semiconductor photocatalysts. In contrast to the conflicting reports of doping or modifying semiconductors with transition metal ions, in general, the photocatalytic activities of rare earth modified semiconductors (especially at low loadings) are recognized to be higher than using non-modified semiconductors. Doping TiO_2 nanomaterials with rare earth elements [15–25] showed numerous advantages namely: (i) better TiO_2 thermal stability, (ii) inhibition of TiO_2 crystallite growth, (iii) limitation of the amount of defects and (iv) improvement of the photocatalytic activity. Some researchers attributed the increased photocatalytic activity to a decrease of the electron-hole recombination rate through electron capture by rare earth incompletely occupied 4f and empty 5d orbitals [26–32]. So, among these elements, lanthanum, having $[\text{Xe}]5d^1 6s^2$ electronic configuration, is considered as one of the most interesting element thanks to its simple extraction method. In addition, Lanthanum showed significant improvement on both photocatalytic activity and thermal stability of anatase phase [15–19,22,23]. Furthermore, increasing the proportion of oxygen vacancies at the surface of photocatalytic material resulting from addition of La would have a beneficial effect on the photocatalytic activity [17,18,33–37]. Some of these works [18,35] concluded that oxygen sites vacancies could be considered as electron capture sites forming excitons level which could improve the lifetime of photogenerated holes. In this respect, particle size decrease will increase the content of oxygen vacancies [18,35]. However, this hypothesis remains controversial. Introduction of lanthanum could then be interesting due to its capacity to induce restriction of TiO_2 particle size growth [15–19]. Recently, Nakata and Fujishima [38] found a relationship between the morphology or "design" of the TiO_2 nanomaterials with different physicochemical properties and intended applications. Unfortunately, high recombination rates of photogenerated electron-hole pairs and wide band gap were the main disadvantages that limit photocatalytic activity of TiO_2 materials. One potential solution was to generate 1D TiO_2 nanomaterials with high surface area and expected lower recombination rates resulting from the anisotropic morphology [39]. However, it was found that titanate nanotubes lose their activities after a post thermal treatment at tempera-

tures higher than 500°C [40]. Calcination indeed leads to particle agglomeration and pore collapse resulting in a strong decrease of the surface area limiting the temperature range for which high surface area nanotubes are observed. Doping with rare earth element could be an interesting alternative in this case to increase TiO_2 thermal stability and to maintain good textural properties.

The aim of this work is therefore to study the effect of lanthanum on the structural, textural and morphological properties of TiO_2 nanomaterials obtained from calcination of hydrogenotitanate nanotubes. Addition of lanthanum was first performed using an incipient wetness impregnation method onto hydrogenotitanate nanotubes (HNT). The effect of calcination necessary to obtain the anatase phase on the structural, textural and morphological properties was then investigated as well as the photocatalytic activity for the degradation of formic acid in aqueous solution at ambient conditions. Moreover, the interest of this study will also be focused on the impact of lanthanum and of the post thermal calcination treatment on the electrochemical properties of TiO_2 by using photocurrent experiments to better understand the materials behavior during the photocatalytic process.

2. Materials and methods

2.1. Reagents

Titanium dioxide was provided by Degussa-Hüls AG (TiO_2 (P25), 72% anatase– 28% rutile, $50\text{ m}^2\text{ g}^{-1}$). NaOH and HCOOH were supplied respectively by Fisher Chemicals and Acros Organics. HCl solution was provided by Panreac Quimica SA (37 wt%). $\text{La}(\text{NO}_3)_3 \cdot 6\text{H}_2\text{O}$ was purchased from Sigma–Aldrich (99.99%). Ultrapure water ($18\text{ M}\Omega\text{ cm}^{-1}$) was used throughout the whole experiments.

2.2. Elaboration of lanthanum-doped TiO_2 nanomaterials

In this work, the same protocol proposed in our previous work [40] was used herein to elaborate TiO_2 nanomaterials obtained by calcination of hydrogenotitanate nanotubes (HNT). Typically, HNT solids were first prepared via alkaline hydrothermal treatment. 3.0 g of TiO_2 powder (P25) were treated with 90 mL of a concentrated solution of NaOH (11.25 M) in a 150 mL Teflon-lined autoclave at 130°C for 20 h. The resulting precipitate was separated by filtration and washed with HCl first using a 0.1 M solution and then a 1 M solution followed by ultra-pure hot water washing in order to remove sodium [41,42]. Lanthanum was introduced into HNT material by incipient wetness impregnation method in order to reach a final 1 wt% La loading, optimum for photocatalytic response. Typically: 31.5 mg of $\text{La}(\text{NO}_3)_3 \cdot 6\text{H}_2\text{O}$ was first dissolved in 1 mL of water (equivalent of twice the porous volume of the HNT material) before being contacted with 0.99 g of HNT material under ultrasonic treatment for 5 min. Finally, the as-obtained paste was dried overnight at 80°C . The as-obtained materials are named La–HNT. Finally, the HTNT and La–HNT materials were calcined between 400°C and 700°C under air for 2 h with a flow rate of 10 mL min^{-1} . The calcined materials are named HNT–T and La–HNT–T with T the calcination temperature in $^\circ\text{C}$.

2.3. Samples characterization

The sodium (Na^+) and lanthanum (La^{3+}) amounts were evaluated by inductively coupled plasma optical emission spectrometry (ICP-OES) measurements using a Horiba Jobin Yvon Activa apparatus. Before analysis, samples were submitted to an acid attack by a mixture of H_2SO_4 , HNO_3 and HF (1:1:0.5, v/v/v ratio) followed by maximum evaporation.

Nitrogen adsorption–desorption isotherms at 77K were obtained on a Micrometrics ASAP 2020 nitrogen adsorption apparatus. The Brunauer–Emmett–Teller specific surface areas (S_{BET}) were determined by a multipoint BET method using the adsorption data in the relative P/P^0 pressure range of 0.05–0.25. Pore size distributions was evaluated by desorption isotherms using the Barrett–Joyner–Halenda (BJH) method. Determination of total pore volumes was performed using nitrogen adsorption volumes at relative pressure (P/P^0) of 0.95.

The identification of the phases in the sample was determined by X-ray diffraction using a Bruker D8 Advance A25 diffractometer with $\text{CuK}\alpha$ radiation ($\lambda = 1.54184 \text{ \AA}$) and using the High Score Plus software.

Raman spectra were treated using a LabRAM-HR instrument at 20°C (Horiba JobinYvon) from 100 cm^{-1} to 1000 cm^{-1} . Spectral resolution was set to 4.0 cm^{-1} . A 514 nm argon-krypton RM 2018 laser as incident light and a CCD detector cooled at -75°C were used. The average power at the surface of samples was set at 1 mW.

The morphology of elaborated materials was studied using transmission electron microscopy (TEM) images acquired with a JEOL 2010 microscope operating at 200 kV. The instrument was equipped with an ultra-high resolution polar piece (point resolution: 1.9 \AA). Samples were prepared by dropping and drying the colloidal solution onto a holey carbon film supported on a Cu grid (300 meshes).

Energy band gap (E_g) values were determined by UV–vis diffuse reflectance spectroscopy (DRS) using an AvaSpec-2048 Fiber Optic Spectrometer equipped with a symmetrical Czerny–Turner design configuration with 2048 pixel CCD detector array. Spectra were recorded from 250 nm to 800 nm and barium sulfate (BaSO_4) was used as a blank white reference.

The photoluminescence spectra were recorded with a spectrofluorophotometer (PerkinElmer LS55 equipped with a Xenon lamp (200–700 nm)) using two excited wavelength around 330 nm and 380 nm.

Photocurrent experiments were conducted using a VoltaLab 40 PGZ301 potentiostat (Radiometer Analytical) and using VoltaMaster 4.0 software for data acquisition. A 100 mL cell made of quartz was used as the photoelectrochemical cell with catalyst films deposited on ITO glass plate as working electrode, a Pt counter electrode and a saturated calomel reference electrode (SCE). All potentials are quoted versus SCE. The geometric surface of the working electrode was 1 cm^2 . The electrolyte was an air-saturated aqueous solution with 0.1 M NaOH. A 150W Xenon lamp (intensity = 1 mW cm^{-2}) was employed as a UV excitation source ($\lambda = 365 \text{ nm}$).

2.4. Formic acid photocatalytic degradation test

2.4.1. Photoreactor and light source

The batch photoreactor is a cylindrical flask made of Pyrex of ca. 100 mL with a bottom optical window of ca. 4 cm in diameter which was open to air. Irradiation was provided by a high pressure mercury lamp (Philips HPK 125W) which provides maximum energy at 365 nm. An optical filter Corning 0.52 was installed to cut off wavelength below 340 nm. The circulating-water cell (thickness: 2.2 cm) was used to remove IR radiation thus preventing any heating of the suspension. The radiant flux was measured with a VLX-3W radiometer with a CX-365 detector (UV-A). The distance which separates the photoreactor from the water cell is regulated all time in order to preserve the radiant flux constant at $5.0 \pm 0.2 \text{ mW cm}^{-2}$ for all photocatalytic tests. At different times of photoreaction, samples were taken with 1 mL syringe and filtered using 0.45 μm Millipore filters to remove TiO_2 particles before analysis.

2.4.2. Formic acid addition

A volume of 30 mL of FA (from 109 to $6517 \mu\text{mol L}^{-1}$) was introduced into the photoreactor with 30 mg of TiO_2 photocatalyst (1 g L^{-1}). The mixture was stirred under dark conditions during 30 min. This time is necessary to reach adsorption–desorption equilibrium conditions. The photocatalytic degradation tests of FA were carried out at room temperature and at natural pH (ca. 3.5). In order to study the adsorption phenomenon and the photodegradation kinetics, different concentrations of FA were used.

2.4.3. Analytical determination

The concentrations of FA remaining after adsorption and during the photocatalytic degradation process were determined using HPLC analysis. VARIAN Prostar HPLC apparatus equipped with a single wavelength UV–vis detector and a $300 \text{ mm} \times 7.8 \text{ mm}$ carbohydrate analysis column (COREGEL-87H3) were used. The mobile phase was an H_2SO_4 solution ($5.10^{-3} \text{ mol L}^{-1}$) and the flow rate was fixed at 0.7 mL min^{-1} . The detection wavelength was set at 210 nm.

3. Results and discussion

3.1. Elemental analysis

ICP analysis was performed to determine the amounts of La and of residual sodium in our materials. After washing the HNT material with HCl (1 M) and ultrapure water, the residual sodium content reaches a very low value (ca. 0.18 wt%). It was shown previously [40] that the presence of sodium (i) could retard the anatase phase formation and (ii) has an inhibitory effect on the photocatalytic activity of materials because it was considered as a recombination site during the photocatalytic process. For this reason, washing with acid (1 M) is an important step to achieve final highly photocatalytically active TiO_2 materials. Using the wet impregnation method, the desired quantity of La (1.01 wt%) is achieved with success.

3.2. X-ray diffraction

The as-synthesized HNT sample presents broad diffraction peaks mainly at 2θ values of 10.0° , 24.6° , 28.4° , and 48.5° which can be ascribed neither to anatase nor to rutile (Fig. 1A). These XRD patterns correspond to an orthorhombic phase of the type $\text{H}_2\text{Ti}_2\text{O}_5 \cdot \text{H}_2\text{O}$ (or $\text{Na}_x\text{H}_2\text{Ti}_2\text{O}_5 \cdot \text{H}_2\text{O}$ for Na-TNT) [43–45]. The main diffraction peaks are then assigned to the (200), (110), (310), (020), and (002) reflections of this orthorhombic phase showing lattice parameters of $a = 18.03$, $b = 3.78$, and $c = 2.99 \text{ \AA}$ [46]. Complementary Rietveld analysis of this sample excludes the possibility of formation of the $\text{H}_2\text{Ti}_3\text{O}_7$ phase as reported in previous studies [47,48].

The diffractograms of calcined HNT and La-HNT at 400°C show essentially similar contributions with characteristic diffraction peaks of anatase at 2θ values of 25.4° , 38.1° , 48.3° , 54.0° , 55.1° and 62.8° ascribed to the (101), (004), (200), (105), (211) and (204) reflections (Fig. 1A). Therefore, the calcination treatment contributes to the phase transformation from the orthorhombic $\text{H}_2\text{Ti}_2\text{O}_5 \cdot \text{H}_2\text{O}$ phase into anatase. However, higher anatase crystallinity can be noticed for La-free nanomaterials.

The evolution of the XRD patterns of HNT and La-HNT samples with increasing temperature of calcination is reported in Fig. 1B and C respectively. Results demonstrate that La doping can influence the structural evolution of TiO_2 materials during calcination. In particular, lanthanum influences the calcination temperature at which the rutile phase starts being formed.

Indeed, for La-free nanomaterials, the diffraction peak at $2\theta = 27.7^\circ$ relative to the rutile phase appears at 600°C and increases dramatically in intensity at 700°C (Fig. 1B). By contrast, the presence of La retards the rutile formation as shown in Fig. 1C.

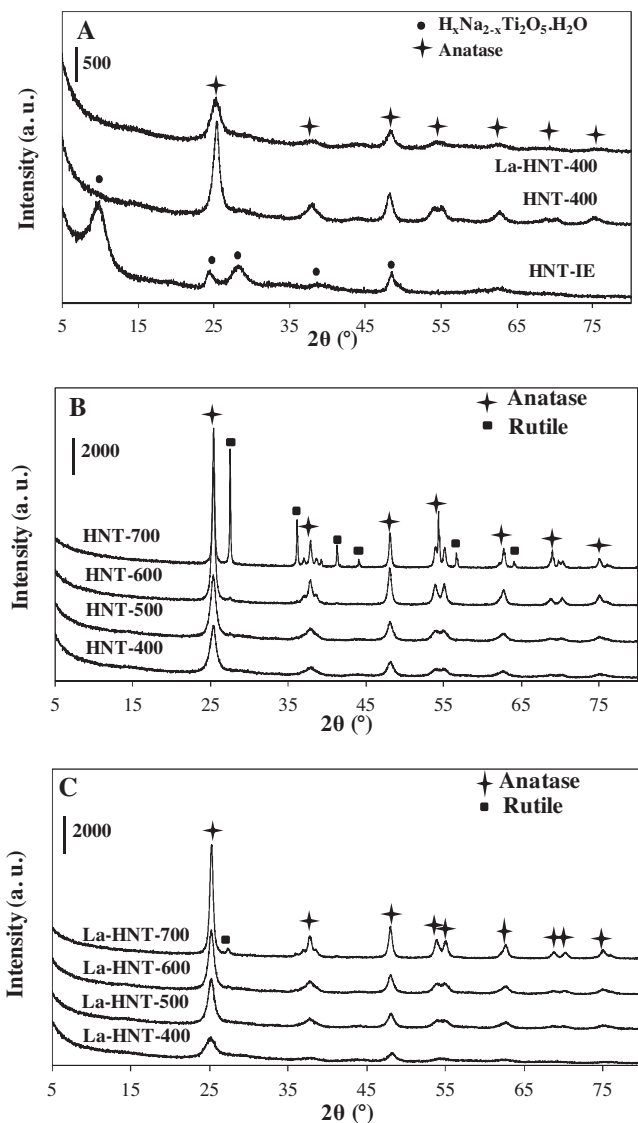


Fig. 1. XRD patterns of: (A) HNT samples at different steps of elaboration, (B) HNT samples after calcination at different temperatures, and (C) La-HNT samples after calcination at different temperatures.

Only a weak XRD signal related to rutile can be detected at 700 °C in good agreement with previous works [15–19,22,23]. The delay in phase transition was explained previously [49] by the formation of Ti–O–La terminations resulting in a higher stabilization of the anatase surface energy therefore restraining the growth of TiO₂ particles and delaying the anatase-rutile transformation to higher temperatures [50]. It can also be noticed that there is no obvious shift of the main (1 0 1) diffraction peak of the anatase phase even after doping with lanthanum (i) indicating the absence of distortion in the TiO₂ lattice [36,51] and (ii) demonstrating that La does not enter into the bulk lattice of TiO₂. This result could be explained by the strong variation in ionic radius between La³⁺ (1.15 Å) and Ti⁴⁺ (0.68 Å).

Furthermore, Huo et al. [17] explained that La₂O₃ species can prevent the agglomeration of TiO₂ nanoparticles during the heat treatment resulting in the inhibition of the phase transformation from anatase to rutile. In our case, the presence of lanthanum oxide is highly probable even if the corresponding diffraction peaks of La₂O₃ are not detected. This result could be explained by the low content of lanthanum which is lower than the detection limit of XRD technique or by a high dispersion of La₂O₃ onto TiO₂ nanoma-

Table 1

Textural properties, band gap energy values and anatase crystallite sizes for undoped and lanthanum-doped TiO₂ nanomaterials.

Catalysts	S_{BET} (m ² g ⁻¹)	V_{meso} (cm ³ g ⁻¹)	E_g (eV)	Anatase crystallite size (nm)
P25	50	0.18	3.20	24.5
HNT-400	214	0.68	3.18	9.0
HNT-500	135	0.55	3.17	11.5
HNT-600	81	0.42	3.15	16.0
HNT-700	30	0.18	2.95	25.0
La-HNT-400	183	0.52	3.13	8.0
La-HNT-500	175	0.67	3.14	9.0
La-HNT-600	143	0.62	3.17	9.5
La-HNT-700	77	0.49	3.18	14.5

terials [52,53]. In addition, doping TiO₂ with rare earth elements like La [15–19,22,23,31,32], Ce [15,20,21,24,25] or other lanthanide elements has a direct impact on the evolution of the crystallite size of the anatase phase. The average anatase crystalline sizes (or more precisely the anatase coherent domains) were then calculated according to line width analysis of the (1 0 1) reflection using the Scherrer equation (Eq. (1)) (Table 1):

$$L = \frac{K\lambda}{\beta_i \cos(2\theta/2)} \quad (1)$$

where L is the crystallite size, K is taken 1, λ is the wavelength of the X-ray radiation ($\text{CuK}\alpha = 0.15406 \text{ nm}$) and β_i is the line width at half-maximum height.

The heat treatment affects TiO₂ crystallites sizes differently depending on the presence of La or not. For La-free nanomaterials, increasing the calcination temperature from 400 °C to 700 °C yields to a significant increase in the anatase crystalline size from 9 nm to 25 nm. By contrast, smaller anatase crystallite sizes (or coherent domains) are obtained for La-doped materials (8.0–9.5 nm) for calcination temperatures between 400 °C and 600 °C. Only, calcining at 700 °C leads to a moderate crystallite size increase to 14.5 nm, still much lower than for its La-free counterpart (25.0 nm). Therefore, lanthanum strongly inhibits TiO₂ crystallite growth. This result is in agreement with Nie et al. [16] who observed that La doping inhibits crystallite size growth. Shi et al. [22] also observed a reduction of crystallite size when lanthanum was added onto TiO₂. Furthermore, Zhang et al. [53] explained the decrease of crystallite size of anatase phase after doping TiO₂ with lanthanum by the segregation of the dopant cations at the grain boundary hindering grain growth and restricting direct contact between them. It can be concluded that doping with lanthanum prevents the increase of crystallite size of the anatase phase and delays the phase transition into rutile.

3.3. Raman spectroscopy

Raman spectra, as illustrated in Fig. 2, show clearly that all samples, except the undoped HNT calcined at 700 °C, are present mainly as anatase in good agreement with XRD results. Characteristic anatase peaks are found at 143, 198, 394, 514 and 638 cm⁻¹ and correspond respectively to the active modes $E_{g(1)}$, $E_{g(2)}$, B_{1g} , A_{1g} and E_g [54]. The Raman spectrum of HNT-700 shows the appearance of additional peaks at 445 cm⁻¹ and 620 cm⁻¹ indicating the presence of the rutile phase confirming X-ray diffraction results. This differs from La-HNT-700 for which the rutile phase is not detected by Raman. This further supports the stabilization of the anatase phase after La addition. Moreover, spectra of doped materials calcined at 400 °C show that La-doping leads to a slight blue shift and broadening of the main $E_{g(1)}$ mode compared to their La-free equivalents (Fig. S1). Moreover, the amplitude of this blue shift tends to change with increasing temperature of calcination. The shift, initially of 1.1 cm⁻¹ after calcination at 400 °C and 500 °C

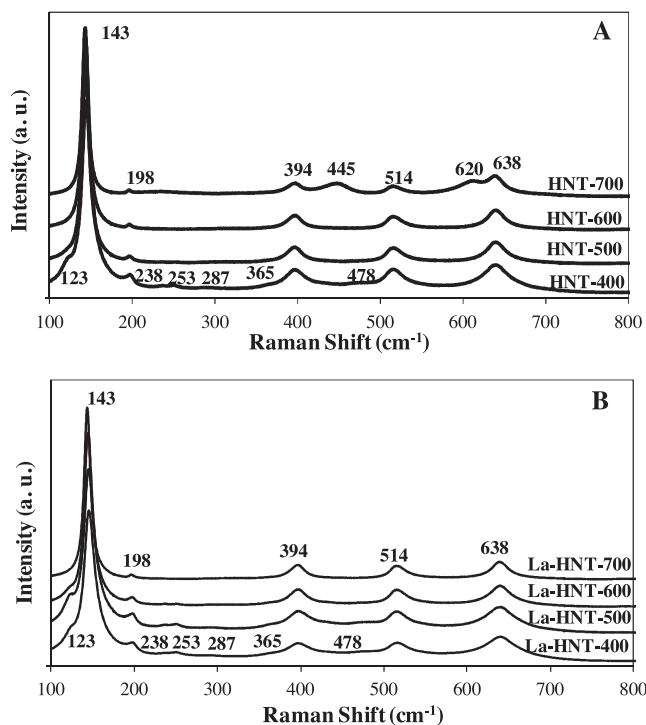


Fig. 2. Raman spectra of HNT (A) and La-HNT (B) materials calcined at different temperatures.

decreases to 0.6 cm^{-1} after treatment at 600°C . Finally, no shift can be detected anymore on the samples treated at 700°C . This blue shift of La-doped samples compared to their La-free counterparts at a given temperature of calcination is also accompanied by a general tendency of all samples to progressively shift to lower wavenumbers with increasing temperature of calcination (of about 2.3 cm^{-1} for La-HNT materials between calcination treatments at 400°C and 700°C and of about 1.1 cm^{-1} for HNT materials). This shift to lower wavenumbers, more important on La-doped samples, was ascribed by Huo et al. [17] to the formation of oxygen surface vacancies whose proportion seems higher on La-doped samples. Moreover, careful examination of Raman spectra shows the presence of low intense contributions at $123(\text{sh})$, 238 , 253 , 287 , $365(\text{sh})$, and 478 cm^{-1} on both HNT-400 and La-HNT-400. These bands are related to the presence of the $\text{TiO}_2(\text{B})$ phase [55]. Other contributions of the $\text{TiO}_2(\text{B})$ phase at 149 , 196 , and 400 cm^{-1} cannot be observed since overlapping with bands of anatase. Moreover, some differences can be noted between La-doped and La-free samples about the relative intensity of $\text{TiO}_2(\text{B})$ contributions. Indeed, if giving relatively similar intensity for both La-HNT-400 and HNT-400, the $\text{TiO}_2(\text{B})$ phase contribution remains clearly detectable on La-HNT-500 while it is hardly discernible for HNT-500. After treatment at 600°C , the $\text{TiO}_2(\text{B})$ phase signal declines on La-HNT-600 even if still detectable while it disappears completely on HNT-600. For both HNT-700 and La-HNT-700, the $\text{TiO}_2(\text{B})$ phase cannot be observed anymore in both cases. This shows that the $\text{TiO}_2(\text{B})$ phase is maintained at higher temperatures of calcination on La-containing samples. This also confirms, in agreement with our previous study [40], a progressive transformation from hydrogenotitanate to $\text{TiO}_2(\text{B})$ and finally anatase with increasing temperature of calcination.

3.4. UV-vis diffuse reflectance spectroscopy (DRS)

UV-vis spectra (Supplementary data, Fig. S2) show a strong absorption in the UV region with no remarkable difference between

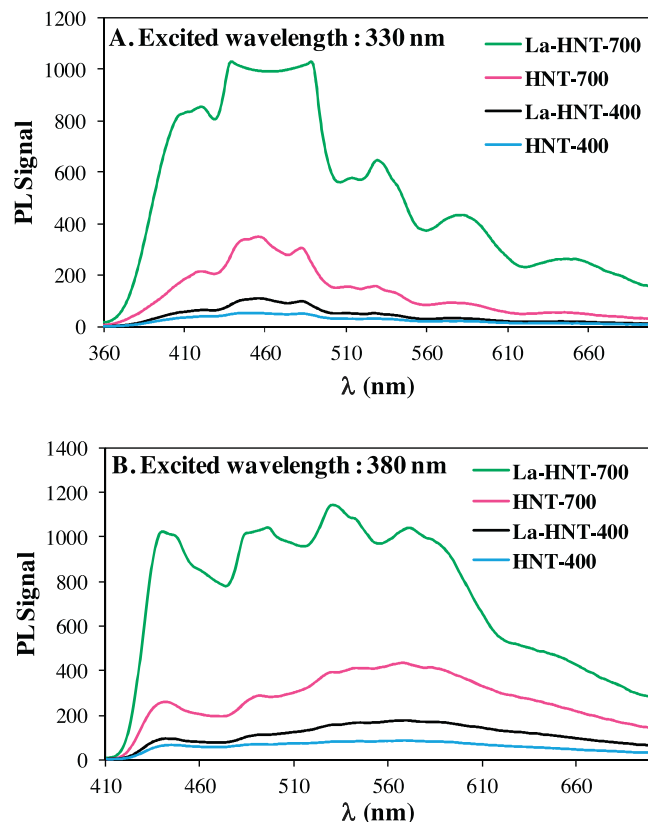


Fig. 3. PL Spectra of HNT and La-HNT samples calcined at 400°C and 700°C using excited wavelengths at 330 nm (A) and 380 nm (B).

undoped and doped materials for calcination temperatures lower or equal to 600°C . However, a higher thermal post-treatment at 700°C leads to a red shift for HNT-700 as expected when a significant transformation of anatase into rutile occurs [56]. By contrast, the UV-vis profile of La-HNT-700 does not show any modification.

The band gap energy (E_g) values of all the samples were determined using the Kubelka–Munk method: $F(R)/h\nu^{1/2}$ versus $h\nu$ plots were built with $F(R) = (1 - R)/2R$ assuming indirect band gap transition. The undoped HNT-T materials calcined between 400°C and 600°C show an average band gap energy value of about 3.17 eV , close to the one expected for anatase [44]. Increasing the post-treatment up to 700°C yields to a slightly lower E_g value of 2.95 eV in agreement with the presence of the rutile phase [56]. However, the band gap energy of La-HNT-T nanomaterials remains unchanged ($\sim 3.15\text{ eV}$) whatever the post-thermal treatment showing the stabilization of the anatase phase at high temperature of calcination.

3.5. Photoluminescence spectroscopy

Fig. 3 reports the photoluminescence (PL) spectra of the La-doped and undoped TiO_2 nanomaterials after calcination at 400°C and 700°C using two excited wavelengths at 330 nm (Fig. 3A) and 380 nm (Fig. 3B). Comparison of the results acquired for the two excited wavelengths shows that lanthanum did not induce new luminescent phenomenon but affects only the PL intensity signal. Moreover, careful analysis of PL spectra acquired at an excited wavelength of 330 nm allows to discern five main contributions. A UV emission peak at 380 nm due to phonon assisted indirect transition from edge (x) to the center (Γ) of the Brillouin zone [57]. An emission contribution around 430 nm is related to trapped elec-

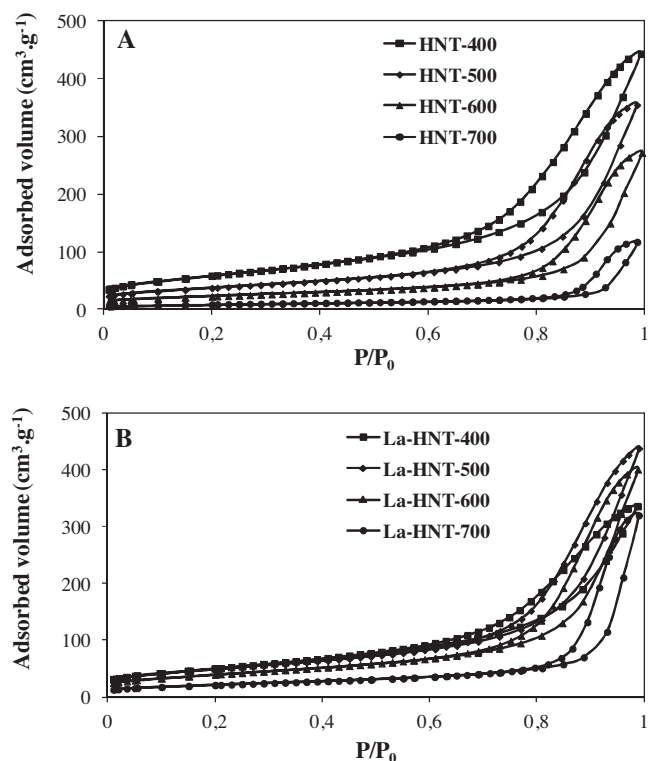


Fig. 4. N_2 adsorption-desorption isotherms of HNT (A) and La-HNT (B) materials calcined at different temperatures.

trons recombining with holes inside the bulk lattice of TiO_2 [58,59]. On the opposite, emission peaks around 460 nm and 535 nm are due to recombination of photogenerated electrons with surface oxygen defects [59]. Finally, the emission peak around 490 nm is due to charge transfer from Ti^{3+} to TiO_6^{2-} octahedra [60].

The low PL intensity of the samples calcined at 400 °C does not allow to qualitatively analyze the different contributions present on the respective spectra. However, after calcination at 700 °C, lanthanum induces an increase of all the different contributions contributing to the PL spectra (bulk recombination, phonon transition, charge transfer and surface oxygen defects). However, the much more discerned peak around 535 nm for La-HNT-700 compared to its La-free counterpart shows that the contribution coming from surface oxygen defects is more significant on the La-doped sample. PL spectra results acquired using a 380 nm excited wavelength leads to essentially similar conclusions but with an expected shift to higher wavelength values of the five main contributions.

Summarizing these results, PL emission spectroscopy shows that increasing the temperature of calcination to 700 °C leads as expected to stronger emission peaks related to bulk recombination or recombination with surface oxygen vacancies. However, using lanthanum as dopant leads apparently to a more significant contribution from surface oxygen defects.

3.6. Textural properties

In order to study the effect of lanthanum doping and of the subsequent calcination treatment on the textural properties of HNT nanomaterials, a set of N_2 adsorption-desorption measurements were carried out as shown in Fig. 4. All isotherms are a type IV profile with H3 hysteresis loops which is characteristic of non-rigid particles aggregates giving rise to pores in the form of slot [40]. BJH pore size distributions (Supplementary data, Fig. S3), shift progressively to higher pore diameter values after calcination for both La-doped and La-free TiO_2 nanomaterials. After calcination at 400 °C, the sur-

face areas of HNT and La-HNT materials (Table 1) show a slight decrease of the surface area from $214 \text{ m}^2 \text{ g}^{-1}$ to $183 \text{ m}^2 \text{ g}^{-1}$ after doping with lanthanum. This suggests that some porosity is partially blocked by the presence of La ions. BJH pore size distributions of HNT-400 and La-HNT-400 present a maximum around 9.0 nm with a shoulder at 3.5 nm. The smallest pore size contribution is related to the inner diameter of a nanotubular structure (as confirmed in the next section using TEM) while the highest pore size maximum is due to intergranular porosity resulting from the tendency of HNT materials to form aggregated bunches due to Van der Waals interaction [7,61–62]. Increasing the temperature of calcination led in both cases to progressive shift to higher P/P_0 values of the onset of the hysteresis loops which become progressively less marked. However, some differences can also be noted between the calcined samples prepared in the presence or not of lanthanum. First, the shift to higher P/P_0 values of the onset of the hysteresis loops is more rapid for HNT samples than for La-HNT ones (Fig. 4). This is confirmed by BJH pore size distributions showing that a significant interporosity of the La-HNT samples was maintained at higher temperatures of calcinations while porosity almost completely collapses at a temperature of calcination of 700 °C for HNT samples.

After calcination at 500 °C, the surface area of the HNT-500 sample decreases to $135 \text{ m}^2 \text{ g}^{-1}$ while for La-HNT-500, the surface area remains hardly unchanged ($175 \text{ m}^2 \text{ g}^{-1}$). This result suggests that the presence of La helps in better stabilizing the textural properties when increasing the temperature of calcination. Indeed, for higher temperatures of calcination ($T^\circ \geq 600^\circ \text{C}$), the decrease in surface area is more rapid for HNT samples than for La-HNT ones (Table 1). Lower values were reached for HNT-600 and HNT-700 than for La-HNT-600 and La-HNT-700 (respectively $81 \text{ m}^2 \text{ g}^{-1}$ and $153 \text{ m}^2 \text{ g}^{-1}$ at 600 °C, $30 \text{ m}^2 \text{ g}^{-1}$ and $77 \text{ m}^2 \text{ g}^{-1}$ at 700 °C). Similarly, pore volume values decrease in a similar fashion than surface areas, especially, for HNT materials. However, once again, the pore volume values for La-HNT samples remain higher at a given temperature of calcination as compared to their La-free counterparts.

3.7. Transmission electron microscopy

To study the morphological characteristics of La-HNT materials, TEM micrographs are reported in Fig. 5A–F for La-doped and La-free samples calcined respectively at 400 °C and 700 °C. Our previous study [40] showed that hydrogenotitanate nanotubes, obtained after complete removal of sodium, present a nanotubular morphology with a diameter around 10–14 nm and a wall thickness of 2–3 nm. After calcination at 400 °C for 2 h, the nanotubular morphology is maintained for HNT-400 and typical TEM pictures show that nanotubes are present as aggregated forming voids between them (Fig. 5A) leading to the formation of intergranular porosity. After calcination at 700 °C (Fig. 5B), the HNT-700 sample has completely lost its monodimensional morphology leading to the formation of plate-like particles ($22.3 \pm 0.6 \text{ nm}$) and of nanorods (length = $44.0 \pm 1.1 \text{ nm}$ and width = $15.0 \pm 0.6 \text{ nm}$) (Fig. 5C). Interestingly, the width of these plate-like particles correspond to the size expected when unfolding nanotubes of 8–10 nm diameter suggesting that these plate-like objects are directly formed by rupture of the nanotubes followed by an unfolding process. Lattice fringes are clearly discernible after calcination at 700 °C (inset Fig. 5C) suggesting a relatively high crystallinity. An interlayer d spacing of 0.35 nm can be measured corresponding to the (1 0 1) plane of anatase.

Meanwhile, for La-containing samples, after calcination at 400 °C, the nanotubular morphology is still observed for La-HNT-400 (Fig. 5D) showing that La does not influence the formation of nanotubes by itself. However, smaller plate-like particles ($18.0 \pm 0.7 \text{ nm}$) and nanorods (length = $30.5 \pm 1.1 \text{ nm}$ and

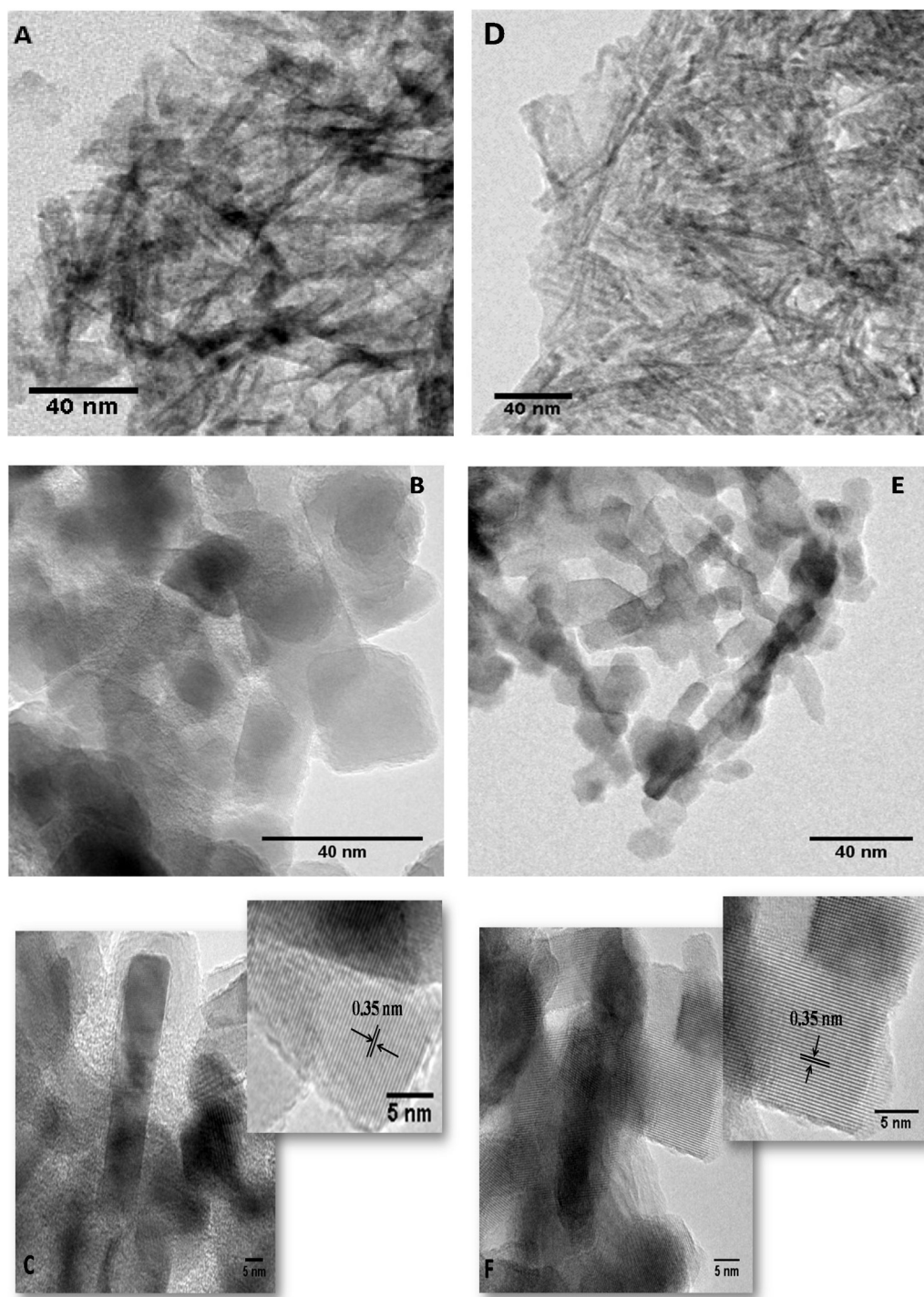


Fig. 5. TEM images of HNT after calcination at 400 °C (A) and 700 °C (B, C) and La-HNT after calcination at 400 °C (D) and 700 °C (E, F). Inserts in C and F show HRTEM images corresponding to fringes of the (1 0 1) plane of anatase.

width = 10.7 ± 0.4 nm) are observed after calcination at 700 °C (Fig. 5E and F). This smaller size of the plate-like particles resulting from the unfolding of TiO_2 nanotubes suggest that lanthanum however did not influence nanotube formation but impacts the size of the nanotubes by restricting their monodimensional growth. Finally, high resolution image of La-HNT-700 (insert Fig. 5F) confirms the presence of lattice fringes corresponding to the (1 0 1) plane of anatase.

3.8. Photocurrent characterization

The lifetime evaluation of photogenerated electron-hole pairs during the photocatalytic process was performed by photocurrent measurements carried-out at 1 V, a potential value at which saturation of the photocurrent can be neglected. Photocurrent results are presented in Supplementary data Fig. S4. Herein, reacting species are specifically OH^- ions coming from the NaOH electrolyte and adsorbed on the surface of the working electrode. The effect of lan-

thanum can be clearly identified after calcination at 700 °C. In that case, the response was highly enhanced for La-HNT-700 compared to its undoped counterpart. This response was directly linked to the lifetime of generated electron-hole pairs. Therefore, the presence of lanthanum effectively decreases the bulk recombination rate through formation of surface oxygen vacancies enhancing the photocatalytic activity of this catalyst. This result confirms Raman and PL spectroscopy results about a more significant formation of surface oxygen vacancies on La-doped samples. However, the photocurrent response was much less pronounced when the calcination treatment was performed at 400 °C for both HNT-400 and La-HNT-400 samples showing (1) that the proportion of surface oxygen vacancies strongly increases with the temperature of calcination in agreement with PL results and (2) that at a calcination temperature of 400 °C, lanthanum does not play any significant role. This point will be confirmed by subsequent photocatalytic experiments.

3.9. Photocatalytic evaluation

The activity of the HNT and La-HNT samples calcined at different temperatures was evaluated for the photodegradation of formic acid (FA). Fig. S5 reports the evolution of the amount of formic acid in solution ($[FA]_0 = 50 \text{ mg L}^{-1} = 1087 \text{ } \mu\text{mol L}^{-1}$) in the dark and with UV illumination. Results only show a negligible decrease of the FA concentration in the dark by adsorption of formic acid. After UV irradiation, a very different comportment can be observed when comparing HNT and La-HNT samples. For HNT samples, the photocatalytic degradation rate tends to decrease when increasing the temperature of calcination from 400 °C to 700 °C. On the opposite, on La-HNT materials, after an initial increase of the degradation rate when increasing the temperature of calcination from 400 °C to 500 °C, almost similar rates were observed for temperatures of calcination higher than 500 °C.

The determination of the initial rate (r_0) of degradation for different initial FA concentrations (from 109 to 6517 $\mu\text{mol L}^{-1}$) allows asserting the kinetic behavior of HNT and La-HNT samples in FA photocatalytic degradation. Initial rates of degradation (r_0) in function of FA concentration are presented in Fig. 6. At low FA concentration, the initial rate of degradation increases as a function of the FA concentration in solution. However, above roughly 2000 $\mu\text{mol L}^{-1}$, all curves tend to level off and reach progressively a plateau. These curves can be further fitted well to a Langmuir-Hinshelwood model according to:

$$r_0 = \frac{kKc_e}{1 + Kc_e} \quad (3)$$

where r_0 is the initial rate of degradation, k is the rate constant of formic acid degradation and K is the adsorption constant of FA onto HNT nanomaterials.

Rate constant values can then be determined and results are summarized in Table 2. For HNT materials, rate constants decrease first slowly with the temperature of calcination (from 400 °C to 500 °C) before reducing more severely above 600 °C, the activity of HNT-700 being only one third of HNT-400. For La-HNT materials, on the opposite, the activity increases by about 40% when increasing the temperature of calcination from 400 °C to 600 °C before stabilizing above 600 °C. As a result of such an opposite evolution versus the temperature of calcination, if HNT samples are more active than La-HNT samples at a temperature of calcination of 400 °C, at $T \geq 600$ °C, La-HNT samples are more photocatalytically active than their La-free counterparts, the highest rate constants being observed for La-HNT-600 and La-HNT-700. Moreover, similar adsorption constant values K (Table 2) only moderately increase with the temperature of calcination for La-HNT samples while K

values strongly decrease for HNT materials showing a complete different kinetic behavior when doping by lanthanum was performed.

As already observed before, lanthanum tends to restrain the crystalline growth of anatase domains when increasing the temperature of calcination, therefore, one could try to determine if variations of photocatalytic activity can be always assigned to the evolution of the crystallite size. One way to evaluate such an effect is based on the determination of the charge carrier migration time (τ) toward the surface of the semiconductor which is size dependent and can be expressed as:

$$\tau = \frac{R^2}{11D} \quad (4)$$

where R is the radius of a particle and D ($5 \cdot 10^{-3} \text{ cm}^2 \text{ s}^{-1}$) [63] is the diffusion coefficient of excited charge carriers.

τ values tend to increase markedly (Table 2) in function of the temperature of calcination for HNT materials going from 12.8 ps for HNT-400 to 99.5 ps for HNT-700. P25 shows a τ value of 95.5 ps versus 99.5 ps for HNT-700, due to bulk recombination. This longer time for charge carriers to migrate to the surface of the semiconductor makes bulk recombination rate strongly increase with increasing temperature of calcination. On the opposite, τ values hardly increase for La-HNT samples up to a temperature of calcination of 600 °C (from 10.2 ps to 14.4 ps) while a moderate increase to 33.4 ps is found for La-HNT-700. However, even if comparison between τ values and rate constants k sustain an indirect role of lanthanum by restraining crystallite growth of anatase domains limiting bulk recombination rate particularly at intermediate temperatures of calcination (up to 500–600 °C), the increase of τ for La-HNT-700 does not correlate with the maintaining of a high rate constant at a temperature of 700 °C. Then, other parameters than only the TiO_2 crystallite size must be involved to completely describe the evolution of the photocatalytic activity of La-HNT materials with the temperature of calcination.

When either the hole or the electron is trapped by surface adsorbed species on the photocatalyst or by an appropriate acceptor, the non-trapped electrons or holes might react with suitable acceptor molecules in solution. The overall reaction will then be decomposed into two steps:

- (1) Formation of an encounter complex between the electron (or hole) acceptor and the semiconductor particle through for example formation of surface oxygen vacancies. The rate of this process will be diffusion limited.
- (2) Interfacial electron transfer (an electrochemical step) involving a Faradic current across the semiconductor-solution interface and characterized by a rate parameter (in cm s^{-1}).

A detailed kinetic treatment of the above reaction steps has been carried out by Marcus [64] who derived the following equation:

$$\frac{1}{k_{\text{obs}}} = \frac{1}{4\pi R^2} \frac{1}{(k_{\text{ct}})} + \frac{R}{D} \quad (5)$$

where R is the sum of the radii of the semiconductor particle and the electron (or hole) and D is the sum of their respective diffusion coefficients, k_{obs} is the classical rate constant obtained experimentally and k_{ct} is the electrochemical rate parameter.

If the heterogeneous charge transfer is considered as much faster than diffusion ($k_{\text{ct}} \gg D/R$). In this case, the well-known Smoluchowski expression is obtained from Eq. (5):

$$k_{\text{obs}} = 4\pi RD \quad (6)$$

k_{obs} values are provided in Table 2 and can be used to determine if reaction rates are diffusion limited or not. Results showed clearly a strong impact of La on the photocatalytic process. Comparison between k_{exp} and k_{obs} values determined from Eq. (6) shows

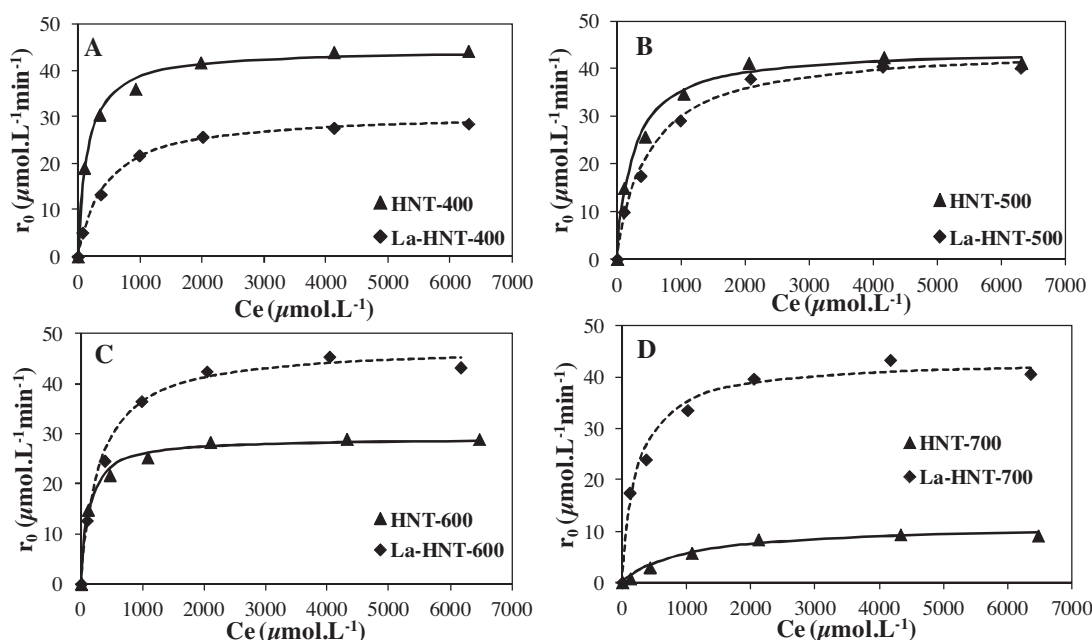


Fig. 6. Comparative degradation kinetics of formic acid for HNT and La-HNT samples calcined at 400 °C (A), 500 °C (B), 600 °C (C) and 700 °C (D).

Table 2

Rate constant values (k_{exp}), adsorption constant (K), and fit accuracy using a Langmuir–Hinshelwood linearization model for the formic acid degradation using undoped and lanthanum-doped TiO_2 nanomaterials. Comparison is also provided with rate constant k_{obs} values obtained by considering that the heterogeneous charge transfer is much faster than diffusion (see text for more information). Charge carrier migration time τ values are also included.

Catalysts	Pseudo-first-order kinetics parameters				R^2
	k ($\mu\text{mol L}^{-1} \text{min}^{-1}$)			K ($\text{L } \mu\text{mol}^{-1}$) 10^{-3}	
	k_{exp}	$k_{\text{obs}}^{\text{a}}$	τ (ps) ^b		
P25	22.0	103.4	95.5	5.9	0.9865
HNT-400	43.5	38.0	12.8	7.9	0.9902
HNT-500	41.5	48.5	21.0	5.2	0.9820
HNT-600	30.0	67.5	40.7	5.5	0.9844
HNT-700	13.6	105.5	99.5	0.6	0.9966
La-HNT-400	31.5	33.7	10.2	2.0	0.9961
La-HNT-500	39.5	38.0	12.8	2.0	0.9764
La-HNT-600	44.8	40.1	14.4	3.0	0.9908
La-HNT-700	44.8	61.1	33.4	4.0	0.9879

^a $k_{\text{obs}} = 4\pi\text{IDR}$.

^b τ (ps) charge carrier.

relatively similar values after calcination at 400 °C for both HNT-400 and La-HNT-400. However, for P25 and HNT materials, with increasing temperature of calcination, k_{obs} values tend to present values much higher than the real k_{exp} values determined experimentally showing that the assumption that the heterogeneous charge transfer being much faster than the diffusion-limiting step involving surface oxygen vacancies. Therefore, for HNT materials, the evolution of experimental rate constants k_{exp} seems related to the evolution of the crystalline growth of anatase domains. Increasing the temperature of calcination induces crystallite growth and higher bulk recombination rate. A very different situation can be found for La-HNT materials. In this case, k_{exp} and k_{obs} values remain relatively similar up to a temperature of calcination of 600 °C while only a moderate over estimation of k_{obs} is observed after calcination at 700 °C. This reveals that in the case of La-doped samples, the assumption that heterogeneous charge transfer is faster than the diffusion step remains valid at all temperatures of calcination. For La-doped samples, the photocatalytic activity response is mainly controlled by the diffusion step related to the formation of complexes between photogenerated electrons and surface oxygen vacancies.

Therefore, the role of lanthanum is related to the formation of surface oxygen vacancies at the TiO_2 surface. Indeed, due to a larger ionic radius, titanium atoms present at the interface could substitute lanthanum atoms in the lattice of La_2O_3 clusters found probably at the TiO_2 surface [34]. Note that the reverse, La substitution inside the TiO_2 lattice is not possible here. Therefore, Ti–O–La bonds could be formed. The replacement however creates charge imbalance leading to formation of surface oxygen vacancies able to capture photogenerated electrons. Hydroxyl ions adsorbed on the TiO_2 surface would then react with the remaining photogenerated holes forming hydroxyl radicals responsible for oxidizing adsorbed FA molecules.

The last question, does lanthanum (or lanthanum oxide) present any intrinsic photocatalytic activity? The incorporation of La ions would lead to the formation of sub-band gap states that lie below the conduction band of the semiconductor [65]. Therefore, the electrons can be excited from the TiO_2 valence band to the La 4f level only by visible light. In our experiments, the irradiation was provided by a high pressure mercury lamp which provides maximum energy at 365 nm; therefore, La species are not photoactive under our experimental conditions. The photocatalytic enhancement is

then more likely due here to the increase of the number of oxygen vacancies and to a lower bulk recombination rate due to restriction of crystallite growth of anatase domains.

4. Conclusion

The effect of lanthanum on the structural, textural, and morphological properties of TiO₂ nanomaterials obtained by calcination of hydrogenotitanate nanotubes was herein studied. Combination of X-ray diffraction, Raman spectroscopy, N₂ adsorption isotherm measurements, photocurrent analysis, UV–vis and photoluminescence spectroscopies allows to determine the influence of lanthanum doping on the photocatalytic response of TiO₂ nanostructured materials. Lanthanum restricts the crystallite growth of anatase domains during the calcination of hydrogenotitanate nanotubes limiting the propensity to form the less photocatalytic active rutile phase at high temperature of thermal treatment. This effect is related to the larger ionic radius of La³⁺ ions which hinders the substitution of La inside the TiO₂ lattice and leading lanthanum (probably present as La₂O₃ clusters) to be well dispersed on the TiO₂ surface. The charge imbalance resulting from the surface incorporation of lanthanum leads to the creation of surface oxygen vacancies whose proportion tends to increase with the temperature of calcination. Kinetic analysis of the formic acid degradation on these La-doped TiO₂ nanostructured materials shows that lanthanum maintains a high level of photocatalytic activity up to high temperatures of calcination contrary to its La-free counterparts whose activity strongly decreases with increasing temperature of thermal treatment. The maintaining of a high photocatalytic activity level results from a combination of effects due to the restriction of the anatase crystallite growth and of a high amount of surface oxygen vacancies limiting the recombination of photogenerated electron-hole pairs.

Acknowledgments

The authors gratefully acknowledge the financial support by the Ministry of Higher Education and Scientific Research in Tunisia and the access to the different physico-chemical techniques and laboratories at the Institut de Recherches sur la Catalyse et l'Environnement de Lyon (IRCELYON) and also access to the laboratory of Centre de Recherches et des Technologies des Eaux, Technopôle de Borj-Cédria (CERTE).

Appendix A. Supplementary data

Supplementary data associated with this article can be found, in the online version, at <http://dx.doi.org/10.1016/j.apcatb.2015.08.037>.

References

- [1] R. Da Silva, L.G.C. Rego, J.A. Freire, J. Rodriguez, D. Laria, V.S. Batista, J. Phys. Chem. C 114 (2010) 19433–19442.
- [2] Z. Sun, J.H. Kim, T. Liao, Y. Zhao, F. Bijarbooneh, V. Malgras, S.X. Dou, Cryst. Eng. Comm. 14 (2012) 5472–5478.
- [3] N. Liu, X. Chen, J. Zhang, J.W. Schwank, Catal. Today 225 (2014) 34–51.
- [4] J. Yu, H. Yu, B. Cheng, C. Trapalis, J. Mol. Catal. A: Chem. 249 (2006) 135–142.
- [5] C. Karunakaran, R. Dhanalakshmi, Sol. Energy Mater. Sol. Cells 92 (2008) 1315–1321.
- [6] C. Karunakaran, P. Anilkumar, J. Mol. Catal. A: Chem. 265 (2007) 153–158.
- [7] J. Araújo, J.M. Doña-Rodríguez, D. Portillo-Carrizo, C. Fernández-Rodríguez, J. Pérez-Peña, O. González Díaz, J.A. Navío, M. Macías, Appl. Catal. B 100 (2010) 346–354.
- [8] S. Liu, N. Jaffrezic, C. Guillard, Appl. Surf. Sci. 255 (2008) 2704–2709.
- [9] S.-J. Tsai, S. Cheng, Catal. Today 33 (1997) 227–237.
- [10] F. Claudel, La Catalyse au Laboratoire et dans L'industrie, MASSON & CIE, Paris, 1967, pp. 45–60.
- [11] H. Tamurah, N. Katayama, Environ. Sci. Technol. 30 (1996) 1198–1204.
- [12] L. Deng, Y. Chen, M. Yao, S. Wang, B. Zhu, W. Huang, S. Zhang, J. Sol-Gel Sci. Technol. 53 (2010) 535–541.
- [13] Y. Su, Y. Deng, Appl. Surf. Sci. 257 (2011) 9791–9795.
- [14] J.M. Herrmann, J. Photochem. Photobiol. A 216 (2010) 85–93.
- [15] M.S. Hassan, T. Amma, O.-B. Yang, H.-C. Kim, M.-S. Khil, Ceram. Int. 38 (2012) 5925–5930.
- [16] J. Nie, Y. Mo, B. Zheng, H. Yuan, D. Xiao, Electrochim. Acta 90 (2013) 589–596.
- [17] Y. Huo, J. Zhu, J. Li, G. Li, H. Li, J. Mol. Catal. A: Chem. 278 (2007) 237–243.
- [18] L. Jing, X. Sun, B. Xin, B. Wang, W. Cai, H. Fu, J. Solid State Chem. 177 (2004) 3375–3382.
- [19] H.R. Kim, T.G. Lee, Y.-G. Shul, J. Photochem. Photobiol. A 185 (2007) 156–160.
- [20] A.M.T. Silva, C.G. Silva, G. Drazic, J.L. Faria, Catal. Today 144 (2009) 13–18.
- [21] N. Aman, P.K. Satapathy, T. Mishra, M. Mahato, N.N. Das, Mater. Res. Bull. 47 (2012) 179–183.
- [22] Z. Shi, X. Zhang, S. Yao, Particuology 9 (2011) 260–264.
- [23] L. Li, H. Zhuang, H. Bu, Appl. Surf. Sci. 257 (2011) 9221–9225.
- [24] W. Xue, G. Zhang, X. Xu, X. Yang, C. Liu, Biochem. Eng. J. 167 (2011) 397–402.
- [25] C. Wang, Y. Ao, P. Wang, J. Hou, J. Qian, S. Zhang, J. Hazard. Mater. 178 (2010) 517–521.
- [26] A.S. Weber, A.M. Grady, R.T. Koodali, Catal. Sci. Tech. 2 (2012) 683–693.
- [27] A.N. Okte, Appl. Catal. A475 (2014) 27–39.
- [28] M. Nasir, S. Bagwasi, Y. Jiao, F. Chen, B. Tian, J. Zhang, Biochem. Eng. J. 236 (2014) 388–397.
- [29] M. Grujic-Brojcin, S. Armakovic, N. Tomic, B. Abramovic, A. Golubovic, B. Stojadinovic, A. Kremenovic, B. Babic, Z. Dohcevic-Mitrovic, M. Scepanovic, Mater. Charact. 88 (2014) 30–41.
- [30] H.-H. Wu, L.-X. Deng, S.-R. Wang, B.-L. Zhu, W.-P. Huang, S.-H. Wu, S.-M. Zhang, J. Dispersion Sci. Technol. 31 (2010) 1311–1316.
- [31] Z.-W. Cheng, L. Feng, J.-M. Chen, J.-M. Yu, Y.-F. Jiang, J. Hazard. Mater. 254–255 (2013) 354–363.
- [32] X. Lan, L. Wang, B. Zhang, B. Tian, J. Zhang, Catal. Today 224 (2014) 163–170.
- [33] P.V. Korake, R.S. Dhabbe, A.N. Kadam, Y.B. Gaikwad, K.M. Garadkar, J. Photochem. Photobiol. B 130 (2014) 11–19.
- [34] D. Xu, L. Feng, A. Lei, J. Colloid Interface Sci. 329 (2009) 395–403.
- [35] M. Ganguly, S.K. Rout, T.P. Sinha, S.K. Sharma, H.Y. Park, C.W. Ahn, I.W. Kim, J. Alloys Compd. 579 (2013) 473–484.
- [36] D.V. Bavykin, J.M. Friedrich, F.C. Walsh, J. Adv. Mater. 18 (2006) 2807–2824.
- [37] H. Zhang, X.P. Ga, G.R. Li, T.Y. Yan, H.Y. Zhu, Electrochim. Acta 53 (2008) 7061–7068.
- [38] K. Nakata, A. Fujishima, J. Photochem. Photobiol. C 13 (2012) 169–189.
- [39] N. Wu, J. Wang, D.N. Tafen, H. Wang, J.G. Zheng, J.P. Lewis, X. Liu, S.S. Leonard, A. Manivannan, J. Am. Chem. Soc. 132 (2010) 6679–6685.
- [40] A. Turki, H. Kochkar, C. Guillard, G. Berhault, A. Ghorbel, Appl. Catal. B 138–139 (2013) 401–415.
- [41] A. Turki, H. Kochkar, I. García-Fernández, M.I. Polo-López, A. Ghorbel, C. Guillard, G. Berhault, P. Fernández-Ibáñez, Catal. Today 209 (2013) 147–152.
- [42] H. Kochkar, N. Lakhdhar, G. Berhault, M. Bausach, A. Ghorbel, J. Phys. Chem. C 113 (2009) 1672–1679.
- [43] B. Vijayan, N.M. Dimitrijevic, T. Rajh, K. Gray, J. Phys. Chem. C 114 (2010) 12994–13002.
- [44] S. Mozia, E. Borowiak-Paleń, J. Przepiórski, B. Grzmil, T. Tsumura, M. Toyoda, J. Grzechulska-Damszel, A.W. Morawski, J. Phys. Chem. Solids 71 (2010) 263–272.
- [45] J. Huang, Y. Cao, M. Wang, C. Huang, Z. Deng, H. Tong, Z. Liu, J. Phys. Chem. C 114 (2010) 14748–14754.
- [46] M. Sugita, M. Tsuji, M. Abo, Bull. Chem. Soc. Jpn. 63 (1990) 1978–1984.
- [47] C.K. Lee, C.C. Wang, M.D. Lyu, L.C. Juang, S.S. Liu, S.H. Hung, J. Colloid Interface Sci. 316 (2007) 562–569.
- [48] E. Morgado Jr., M.A.S. de Abreu, G.T. Moure, B.A. Marinkovic, P.M. Jardim, A.S. Araujo, Chem. Mater. 19 (2007) 665–676.
- [49] H. Zhang, J.F. Banfield, J. Mater. Chem. 8 (1998) 2073–2076.
- [50] J. Zhang, Z. Zhao, X. Wang, T. Yu, J. Guan, Z. Yu, Z. Li, Z. Zou, J. Phys. Chem. C 114 (2010) 18396–18400.
- [51] F.B. Li, X.Z. Li, M.F. Hou, Appl. Catal. B 48 (2004) 185–194.
- [52] F.B. Li, X.Z. Li, C.H. Ao, S.C. Lee, M.F. Hou, Chemosphere 59 (2005) 787–800.
- [53] Y. Zhang, H. Zhang, Y. Xu, Y. Wang, J. Solid State Chem. 177 (2004) 3490–3498.
- [54] M.J. Scepanovic, M. Grujic-Brojcin, Z.D. Dohcevic-Mitrovic, Z.V. Popovic, Appl. Phys. A 86 (2007) 365.
- [55] T. Beuvier, M. Richard-Plouet, L. Brohan, J. Phys. Chem. C 113 (2009) 13703–13706.
- [56] J. Yu, H. Yu, Mater. Chem. Phys. 100 (2006) 507–512.
- [57] N. Serpone, D. Lawless, R. Khairutdinov, J. Phys. Chem. 99 (1995) 16646–16654.
- [58] Y. Lei, L.D. Zhang, G.W. Meng, G.H. Li, X.Y. Zhang, C.H. Liang, W. Chen, S.X. Wang, Appl. Phys. Lett. 78 (2001) 1125–1127.
- [59] J. Preclikova, P. Galar, F. Trojaneš, S. Danis, B. Rezek, I. Gregora, Y. Nemcova, P. Maly, J. Appl. Phys. 108 (2010) 113502.
- [60] J. Liu, J. Li, A. Sedhain, J. Lin, H. Jiang, J. Phys. Chem. C 112 (2008) 17127–17132.
- [61] E. Morgado Jr., M.A.S. de Abreu, G.T. Moure, B.A. Marinkovic, P.M. Jardim, A.S. Araujo, Chem. Mater. 19 (2007) 665–676.
- [62] F. Cesano, S. Bertarione, M.J. Uddin, G. Agostini, D. Scarano, A. Zecchina, J. Phys. Chem. C 114 (2010) 169–178.
- [63] M. Graetzel, A. Frank, J. Phys. Chem. 86 (1982) 2964–2967.
- [64] R.A. Marcus, J. Chem. Phys. 24 (1956) 966–978.
- [65] C. Wang, Y.H. Ao, P.F. Wang, J. Hou, J. Qian, Appl. Surf. Sci. 257 (2010) 227–231.